Journal of Vacuum Science and Technology B

RESEARCH ARTICLE | OCTOBER 30 2024

Fabrication of model ultrafiltration membranes with uniform, high aspect ratio pores

Special Collection: Papers from the 67th International Conference on Electron, Ion and Photon Beam Technology and Nanofabrication (EIPBN 2024)

Wen Chen ; Soonmin Yim ; Nestor J. Zaluzec ; Gordon S. W. Craig ; Seth B. Darling ; Paul F. Nealey

J. Vac. Sci. Technol. B 42, 062803 (2024)
https://doi.org/10.1116/6.0004050
CHORUS

JVST B
Journal of Vacuum Science & Technology B

ARTICLE

pubs.aip.org/avs/jvb

Fabrication of model ultrafiltration membranes with uniform, high aspect ratio pores

Cite as: J. Vac. Sci. Technol. B **42**, 062803 (2024); doi: 10.1116/6.0004050
Submitted: 6 September 2024 · Accepted: 14 October 2024 ·
Published Online: 30 October 2024

Wen Chen,[1,2] Soonmin Yim,[1,2] Nestor J. Zaluzec,[2] Gordon S. W. Craig,[2] Seth B. Darling,[1,2,3] and Paul F. Nealey[1,2,4,a)]

AFFILIATIONS

[1]Advanced Materials for Energy-Water Systems (AMEWS) EFRC, Argonne National Laboratory, 9700 S. Cass Ave., Lemont, Illinois 60439
[2]Pritzker School of Molecular Engineering, The University of Chicago, 5640 S. Ellis Ave., Chicago, Illinois 60637
[3]Chemical Sciences and Engineering Division, Argonne National Laboratory, 9700 S. Cass Ave., Lemont, Illinois 60439
[4]Materials Science Division, Argonne National Laboratory, 9700 S. Cass Ave., Lemont, Illinois 60439

Note: This paper is part of the Special Topic Collection: Papers from the 67th International Conference on Electron, Ion and Photon Beam Technology and Nanofabrication (EIPBN 2024).

[a)]**Author to whom correspondence should be addressed:** nealey@uchicago.edu

ABSTRACT

In this manuscript, we report the facile fabrication of large-area model membranes with highly uniform and high aspect ratio pores with diameters <20 nm. These membranes are useful for fundamental investigations of separation by size exclusion in the ultrafiltration regime, where species to be separated from solution have dimensions of 1–100 nm. Such investigations require membranes with narrow pores and high aspect ratios such that the Hagen–Poiseuille equation is followed, enabling well-known models such as the hindered transport model to be evaluated and other affecting factors to be ignored. We demonstrate that the sub-20 nm pores in the membrane are of sufficiently high aspect ratio such that water flux through the membrane is consistent with the Hagen–Poiseuille equation. The fabrication relies on self-assembling block copolymers to form uniform, densely packed patterns with sub-20 nm resolution, sequential infiltration synthesis to convert the block copolymer *in situ* into a mask with adequate contrast to etch pores with an aspect ratio >5, and low-resolution photolithography to transfer the pattern over a large area into a silicon nitride membrane. Model membranes with narrow pore-size distribution fabricated in this way provide the means to investigate parameters that impact size-selective ultrafiltration separations such as the relationships between solute or particle size and pore size, their distributions, and rejection profiles, and, therefore, test the validity or limits of separation models.

I. INTRODUCTION

Successful separation processes must effectively remove species of different sizes, such as gases, salts, proteins, viruses, and bacteria, from feed streams. Membrane technology has emerged as one of the most promising candidates for many separation processes, including water treatment, gas separation, bioprocessing, and several energy conversion systems.[1,2] Membranes can be categorized based on pore sizes as reverse osmosis (<1 nm), nanofiltration (~1–10 nm), ultrafiltration (UF, ~10–100 nm), and microfiltration (~0.1–5 μm) membranes. In general, the separation performance of a membrane is fundamentally determined by its ability to selectively discriminate between species based on differences in physical and chemical properties. Size exclusion is the primary mechanism that governs selectivity of UF membranes, allowing smaller species to pass through a membrane while larger ones are blocked.[3] When the pore size falls below 10 nm, the separation mechanisms become more complex and additional mechanisms, such as Donnan exclusion and dielectric exclusion, can become dominant to effectively separate target species, mainly charged particles, ions, and gases.[4]

Fundamental investigations of separation by size exclusion in UF membranes are necessary for their effective development and

application. To this end, many models for hindered transport in UF membranes have been developed.[5] The most basic of these models treat the UF membrane as an array of through-film pores in which the fluid flow follows the Hagen–Poiseuille equation.[6] For example, Zeman and Wales developed a hindered transport model, combing both theoretical expressions and experimental results, to characterize the rejection rate based on size while neglecting pore entrance and exit effects and long-range interactions such as van der Waals or electrostatic forces.[7] They showed that particles of different sizes are hindered differently in an infinitely long pore, leading to a distribution in velocity profiles and differences in the concentration of particles upstream and downstream. Waldman *et al.* refined the hindered transport model expressions to demonstrate that controlling the pore-size distribution is crucial for achieving sharp rejection in membrane separations.[8]

Along with mathematical models of the hindered transport process, it is also necessary to have model membranes that precisely replicate the pore geometry in the models. Thus, the model membrane must possess a narrow pore-size distribution, particularly in the sub-20 nm regime, which is critical for accurately testing and refining selective transport principles. Furthermore, the surface chemistry of the membrane must also be thermally stable and chemically inert to maintain its structure and performance over filtration time. Additionally, the membrane thickness needs to be somewhat greater than the pore diameter to ensure Poiseuille flow, but not so great that the permeability of the membrane is negatively impacted. Thus, it is critical to control the aspect ratio of the pores to align with the hindered transport model's requirements. The area of the membrane also needs to be carefully optimized to balance between maintaining its mechanical integrity under the hydraulic pressure of filtration while ensuring adequate permeability. The theoretical flow rates predicted by the Hagen–Poiseuille equation,[8] which assumes a cylindrical pore geometry, can be used to determine whether a membrane meets the requirement for the hindered transport model. Therefore, it is essential to fabricate model membranes that satisfy all the requirements and verify their performance using the Hagen–Poiseuille equation to ensure the accuracy of the pore geometry and flow characteristics.

Impressive efforts have been made to develop UF membranes both for technological applications and fundamental studies of the UF separation models.[9] However, achieving control over the pore-size distribution is nontrivial. Track-etched membranes, a common commercially available option, are prepared by the bombardment of high energy ions into polymeric membranes. These are considered as isoporous membranes with pore sizes of 0.01–30 μm, but the low porosity, low diameter-to-thickness ratio, and overlapping pores of the membranes make them difficult as an ideal platform to study solute transport. An alternative approach that offers total control over the population of pores is to apply nanofabrication principles to membranes.[9,10] Focused-ion-beam milling can directly pattern multiple pores with high resolution and precision in a target material, but it cannot achieve a high aspect ratio (~5) due to the redeposition effect. Electron beam (E-beam) lithography can produce isoporous membranes by templating a porous mask and then transferring its structure to inorganic materials by plasma etching. Although these nanofabrication techniques can create nanopores ranging from a few to several hundred nanometers, the energy and time costs are high for preparing membranes on a large scale. This limitation poses challenges in meeting the requirements for subsequent filtration studies.

As an alternative, synthetic polymeric membranes are widely used in water purification due to their low-cost processing, ease of fabrication, low maintenance, and good separation performance. However, conventional polymer membranes typically have a broad pore-size distribution that limits both their separation performance and their utility in systematically exploring fundamental transport behavior. Block copolymers (BCPs) have the capability to form a variety of nanoscale ordered structures, making them advantageous as structure-directing "templates" for the fabrication of porous membranes.[11] The self-assembly (SA) and nonsolvent-induced phase separation technique of BCPs can create a regularly ordered surface morphology connected strongly with a highly porous substructure and enhanced mechanical stability. However, the tortuous path that forms below the top layer can lead to adsorption and loss of solutes, and the lack of uniformity makes it hard to establish a clear relationship between structure and filtration results.

Many research groups have demonstrated the use of BCPs to make UF membranes. One approach involved the use of a triblock terpolymer that self-assembled into cylinders of one of the blocks.[12] However, to support the terpolymer film, it was necessary to coat the terpolymer film on a nanoporous matrix. Although the flux and selectivity of the UF film were successfully compared to the hindered transport model of Bungay and Brenner,[13] the flux was reduced by the nanoporous support matrix. Similar results were achieved with a terpolymer assembled on a microporous substrate, in which the membrane flux was successfully compared to the Zeman and Wales hindered transport model, but again, flux was decreased due to the microporous substrate.[14] This decrease in flux was also previously observed in a diblock copolymer film deposited on a microporous substrate.[15] Another well-studied approach for fabricating microphase-separated BCP films for UF membranes involved the use of selective swelling of one of the blocks of the BCP and solvent annealing.[16] Although the results achieved with these processes were impressive, such processes require the control of several nonequilibrium processes, such as evaporation, diffusion, solvent–nonsolvent exchange, and the kinetic arrest of microphase separation, which may be undesirable from a manufacturing point of view.[17]

To develop a model membrane with a narrow pore-size distribution suitable for fundamental investigations of size exclusion in the UF regime, we used self-assembled cylinder-forming polystyrene-*block*-polymethyl methacrylate (PS-*b*-PMMA) as a template for the fabrication of nanostructured SiN_x membranes. Sequential infiltration synthesis (SIS) was implemented to grow alumina in the PMMA block to provide the self-assembled BCP structure with etch resistance.[18] The resulting alumina matrix structure was used as the mask to pattern transfer the porous geometry into an SiN_x layer. After KOH anisotropic etching, the membranes were released in the air. Upon completion of the fabrication, SiN_x membranes that were 2.5×0.7 mm^2 in area, 100 nm in thickness, and sub-20 nm in pore size were produced. Compared to the other model polymeric membranes,[12,14] SiN_x membranes have a better mechanical integrity for pressure drops of interest, ~0.4–1.5 psi, to measure flow rate through membranes. The flow rate of the

membranes aligned closely with predictions made by the Hagen–Poiseuille equation, which can be attributed to the aspect ratio of ~5 of the pores.

II. EXPERIMENT

A. Materials

The 500 μm-thick silicon wafers (4-in., N-type, ⟨100⟩ orientation) coated with double side 100 nm low-stress SiN_x were purchased from pure wafer. SiN_x was deposited on the wafers using low-pressure chemical vapor deposition with a stress of less than 250 ± 50 MPa tensile.

PS-*b*-PMMA (M_n = 20.5-*b*-59.0 kg/mol, denoted as C2059, PDI = 1.04, L_0 = 35 nm) and hydroxyl-terminated polystyrene (PS-OH, M_n = 6 kg/mol, PDI = 1.05) were purchased from Polymer Source, Inc. Poly(styrene-*co*-methyl methacrylate-*co*-glycidyl methacrylate) [P(S-*r*-MMA)] random copolymer containing 4 mol. % of glycidyl methacrylate (GMA) and different volume fractions of styrene was synthesized by reversible addition—fragmentation chain transfer polymerization. The random copolymers were abbreviated according to their mole fractions of PS; for example, P(S-*r*-PMMA) with 60 mol. % PS was denoted as 60S. Trimethylaluminum (TMA) was purchased from Strem. All polymer solutions were prepared in toluene and filtered with a polytetrafluoroethylene syringe filter (0.2 μm pore size) purchased from MDI Membrane Technologies.

AZ MiR 703 photoresist and AZ 300 MIF developer were purchased from EMD Performance Materials Corp. AR-P 6200.04 (CSAR 62) E-beam resist was purchased from Allresist. Potassium hydroxide pellets (ACS reagent, 85%) were purchased from Oakwood Products Inc. Gold etchant was purchased from Transene Electronic Chemicals and used as received. ProTEK®B3 Primer was purchased from Brewer Science, Inc. and used as received. PMMA resist (495 kg/mol) was purchased from EM Resist Ltd and used as received. All solvents were purchased from Sigma Aldrich and used as received.

B. Isoporous membrane fabrication

First, photolithography was used to etch a window on the back side of the SiN_x wafers. AZ MIR 703 was spin-coated on the back side of a double-sided SiN_x wafer at 3500 rpm and baked at 95 °C for 1 min. The resist was then patterned in a Heidelberg MLA150 direct write lithographer to prepare the patterns and alignment marks. After developing in the AZ 300 MIF developer for 60 s and rinsing with water, the exposed SiN_x was then etched and removed with CHF_3/O_2 plasma in a PlasmaTherm reactive ion etch (RIE) instrument. The remaining resist was removed with *N*-methyl-2-pyrrolidone (NMP) at 80 °C. The wafer was further cleaned in a Nano-Strip solution at 80 °C for 40 min to remove contamination on the front side and then rinsed with water.

Next, the SiN_x wafer was coated with the P(S-*r*-MMA) containing 60% styrene (denoted as 60S) on the front side, which was designed to be energetically neutral to both blocks of C2059. A 0.3 wt. % solution of 60S in toluene was spin-coated to a thickness of ~11 nm on the frontside. The film thickness was measured with an ellipsometer (J.A. Woollam alpha-SE) using a Cauchy model. The P(S-*r*-MMA) was annealed on a hot plate in an N_2 glovebox for 20 min at 235 °C to cross-link the GMA groups. Then, excess unreacted 60S was removed by ultrasonication in toluene for 5 min, resulting in a slight decrease of the film thickness to ~9 nm. Subsequently, a filtered 2.2 wt. % solution of C2059 in toluene was spin-coated directly onto the wafer to a target film thickness of 91 nm and then thermally annealed at 270 °C for 2 h on a hot plate in a N_2 glovebox. The BCP film was converted into AlO_x nanostructures using SIS, during which the PMMA block reacted with alternating vapor-phase precursors [TMA and de-ionized (DI) H_2O] so that the AlO_x nucleated selectively inside the PMMA domains.

After SIS, 20 nm of gold was deposited on the AlO_x layer using an electron beam evaporator. AZ MIR 703 resist was spin-coated onto the gold layer and baked at 95 °C for 1 min. The resist was then patterned in a direct write lithographer to define the membrane regions on the frontside. After soaking in AZ 300 MIF developer for 60 s and rinsing with water, a 15 s O_2 plasma was applied to remove the residual resist. Then, the SiN_x wafer was baked in an oven at 120 °C for 1 h. Next, the entire SiN_x wafer was soaked in gold etchant for 30 s to expose the AlO_x structure under the gold layer, followed by an O_2 plasma for 10 min in a PlasmaTherm RIE to selectively remove the PS cylinders and a CHF_3-based plasma to etch holes into the underlying SiN_x. After pattern transfer of the cylindrical geometry to the SiN_x, the wafer was soaked in NMP at 80 °C for 15 min to remove the resist. Then, gold etchant was used to remove the remaining gold. Eventually, all of the remaining organic structure was removed with a Nano-Strip solution at 80 °C for 40 min. The wafer was then rinsed with DI water and dried with a N_2 gun.

To release the membrane, the wafer was spin-coated with filtered ProTEK®B3 Primer at 1500 rpm for 60 s and baked on a hot plate at 205 °C for 1 min. Then, the wafer was spin-coated with filtered PMMA resist at 1.5 k rpm and baked on a hotplate at 180 °C for 5 min. The wafer was placed in a wet etch holder (TandemTM from AMMT) with the back side of the pattern exposed, while O-rings sealed off the front side. The setup was immersed in 30 wt. % KOH solution at 80 °C. When there were no further bubbles coming out of the setup (~5 h), the holder was removed from the KOH solution and rinsed with DI water and isopropanol (IPA). After the wafer was removed from the holder and dried, the front side PMMA protection layer was removed with a 15 min O_2 plasma etch.

To use directed self-assembly (DSA) with the BCP, a guiding pattern was created after preparing the neutral layer 60S on the front side of the SiN_x wafer. CSAR 62 resist was spin-coated at 4000 rpm for 45 s and baked at 150 °C for 1 min. A hexagonal close-packed (HCP) array of dots with a pore-to-pore distance, L_s, of 70 nm was written by a Raith EBPG5000 Plus e-beam writer using a 100 kV accelerating voltage, a 10 nA beam current, and a dose of 2000 μC/cm^2. The E-beam pattern was developed in n-amyl acetate for 1 min and an O_2 RIE in a PlasmaTherm RIE instrument was used to etch into the neutral layer 60S for 15 s. The e-beam resist was removed by sonicating in NMP twice for 5 min each and chlorobenzene for 5 min. PS-OH was spin-coated from a 1 wt. % toluene solution at 1500 rpm, and the wafer was baked at 220 °C for 30 min on a hot plate in a N_2 glovebox to graft the

PS-OH brush to the exposed SiN_x film in the e-beam-patterned area. After removing the unreacted brush with NMP and toluene, all the following steps were same with the procedure introduced above.

After fabricating, the 4-in. wafer was cut into 100 $5.4 \times 5.4\ mm^2$ squares, with a $2.5 \times 0.7\ mm^2$ membrane region in the middle of each square. The samples were inspected with top-down scanning electron microscopy (SEM) using a Carl Zeiss Merlin field emission scanning electron microscope and transmission electron microscopy (TEM) images using scanning transmission electron microscopy mode for subsequent metrology and image analysis.

C. Water flux measurement

Both sides of the SiN_x membranes were cleaned for 3 min in an O_2 descumming tool. After optical microscopy inspection to ensure there were no obvious defects, the SiN_x membranes were wetted with IPA and sandwiched in a custom 3D-printed crossflow filtration cell, with the back side of the SiN_x membrane facing the feed side of the cell. Two pressure gauges were installed at the water's inlet and outlet from the 3D-printed cell, and the trans-membrane pressure was calculated to be the average of the readings from the feed and retentate pressure gauges. A polyethersulfone syringe filter with 0.2 μm pore size was used to remove large particles in the DI water. Before beginning the measurement of the water flux, 50 ml of feed water was recirculated within the filtration system for 24 h to stabilize the water flux. The permeating water was collected and weighed on a balance, varying the applied pressure from 0 to 1.5 psi. The steady-state water flux at each applied pressure was calculated by measuring the mass of the permeate as a function of time.

III. RESULTS AND DISCUSSION

A. Membrane fabrication

Schematic illustrations of the isoporous membrane fabrication process are shown in Fig. 1. Cylinder-forming BCPs were used as templates to create porous inorganic structures because they can self-assemble to form arrays of HCP domains. Achieving through-film cylindrical domains oriented perpendicular to the substrate requires thermodynamically favorable conditions for the BCP blocks. This can be achieved in part by creating a chemically or topographically favorable background. We synthesized cross-linkable random copolymers, P(S-*r*-MMA), with 4 mol. % of GMA and varying ratios of PS to PMMA. The composition of the P(S-*r*-MMA) altered the morphology of BCP films at equilibrium.[19,20] Zhou *et al.* studied how annealing temperature, random copolymer composition, and film thickness influenced BCP morphology using PS-*b*-PMMA ($M_n = 20.2$-*b*-50.5 kg mol^{-1}, center-to-center spacing $L_0 = 38.3$ nm).[11] In this work, we used PS-*b*-PMMA with $M_n = 20$-*b*-59 kg mol^{-1} and $L_0 = 35$ nm to grow a thick, perpendicularly oriented nanoporous structure.

The annealing temperature and duration are critical for achieving the desired domain orientation because they alter the interfacial energy of the free surface of the PS and PMMA.[21] To achieve a perpendicular orientation, the interfacial energy of PS and PMMA must be nearly the same, which has been reported to occur at 250 °C.[21] Given that the BCP used in this work had a higher volume fraction of PMMA than PS, we selected 270 °C as the annealing temperature to create a more PMMA-preferential environment. We then studied the time required for the BCP to reach equilibrium. An 80 nm thick PS-*b*-PMMA film was prepared on a Si chip coated with 9 nm of 60S and annealed at 270 °C on a hot plate in a N_2 glovebox, with annealing times of 0.5, 1, 2, and 3 h. The number of parallel defects decreased as the annealing time increased from 0.5 to 3 h (see Fig. S1 in the supplementary material), so we assumed that the BCP films reached near-equilibrium after 2 h at 270 °C.

The chemical composition of the random copolymer played an important role in understanding which conditions allowed cylindrical orientation of BCP. A 90 nm thick PS-*b*-PMMA film was prepared on a Si chip coated with different random copolymer compositions, ranging from 50S to 67S, and annealed at 270 °C for 2 h. The surface morphology progressed from perpendicular cylinders to a mixed orientation of parallel and perpendicular cylinders, with the transition observed at 67S (see Fig. S2 in the

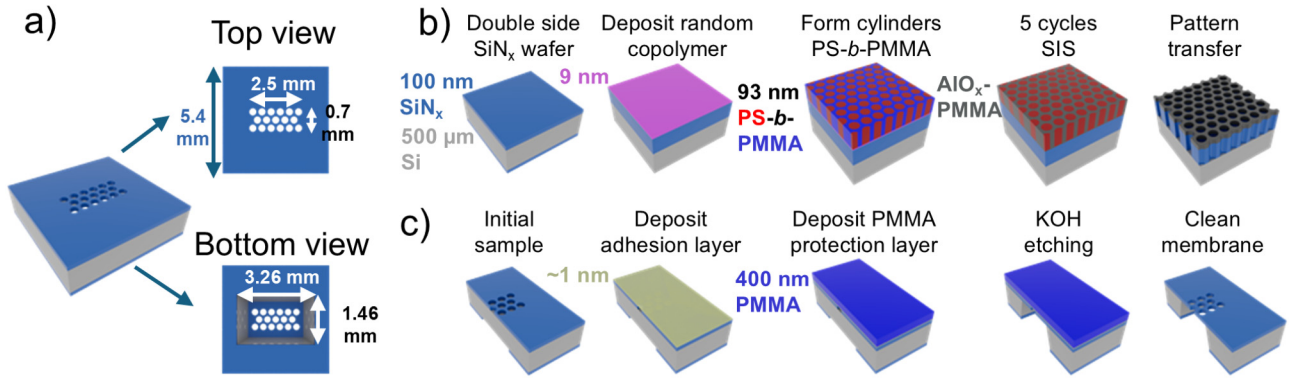

FIG. 1. (a) Overall view of membrane top and bottom. (b) Schematic illustration of the fabrication process of porous structures. (c) Schematic illustration of the membrane releasing process.

supplementary material). The neutral conditions for the cylinder-forming PS-*b*-PMMA were in agreement with previously published work.[11] Finally, 60S was chosen as the random copolymer for subsequent experiments.

Thicker BCP films are desirable as templates due to their higher etching window and improved mechanical properties, necessitating an understanding of the thickness range required for growing perpendicular cylinders. PS-*b*-PMMA films with thicknesses ranging from 86 to 111 nm were compared after spin-coating on a 9 nm 60S substrate, and the surface morphology was imaged after annealing at 270 °C for 2 h (see Fig. S3 in the supplementary material). Parallel cylinders appeared in films thicker than 98 nm, suggesting that in such thick films the surface chemistry of the substrate did not influence domain assembly more than the polymer-free surface interaction. Thus, a thickness of 93 nm was selected as the template because it was the thickest film capable of growing perpendicular cylinders. An SEM image of a 93 nm PS-*b*-PMMA film on 9 nm 60S after annealing at 270 °C for 2 h is shown in Fig. 2(a).

Arrays of nanopores in 30 nm thick SiN_x membranes and Si with different electrical properties were fabricated through the SA and SIS enhancement of cylindrical BCP films.[22,23] Using an atomic layer deposition reactor operating in the semistatic mode, SIS was applied with alternating vapor-phase precursors (TMA and DI H_2O) within a thin film of PS-*b*-PMMA. TMA reacted with carbonyl groups in the PMMA, allowing selective growth of Al_2O_3 in the PMMA domains. Numerous studies have shown that SIS improves the etching resistance of PMMA against plasma, making it a promising technique for creating masks for fabricating nanostructures.[18,24] In this work, we applied five cycles of TMA and DI H_2O sequences to the PS-*b*-PMMA film to ensure sufficient Al_2O_3 nucleation inside PMMA domains. After using an O_2 plasma to selectively remove the PS cylinders, the AlO_x matrix served as the mask for SiN_x [as shown in Fig. 2(a)]. However, adapting previous studies to produce 100 nm thick SiN_x membranes presented challenges. For example, adjusting the etching condition (RF power = 100 W, ICP power = 300 W, CHF_3 flow = 30 SCCM, O_2 flow = 20 SCCM, pressure = 10 mTorr) from previous work[22] to etch through a 100 nm SiN_x film resulted in the SIS structure being etched away and the SiN_x surface being damaged by the plasma (Fig. 3).

The etching mechanism of silicon-based materials has been extensively studied, providing the design logic to find an etching condition with high etch selectivity with respect to AlO_x and SiN_x, flat surface roughness, and straight etching profile.[25] All experiments were completed by etching SiN_x witness samples and SiN_x with five-cycle SIS nanopores simultaneously, with the etching time determined by the complete etching of the SiN_x witness sample. To induce a more anisotropic plasma for straight pores, we increased the ratio of physical sputtering to ion-assisted chemical etching by adjusting to a lower ICP power and higher RF power (RF power = 250 W and ICP power = 100 W), and the etching result was compared with the initial etching result in Fig. 3. The new condition resulted in a more remaining SiN_x structure, indicating increased selectivity between SIS alumina and SiN_x. However, the SiN_x under the SIS structures was still etched, leaving a rough surface. Other factors needed to be considered. Although the PMMA film was enriched with AlO_x, a significant fraction of the organic component remained, which is prone to physical and O_2 etching. Thus, the ratio of O_2 to fluorine-containing gas was lowered and ICP power was increased while decreasing RF power to improve the etch selectivity. The etching condition of RF power = 100 W, ICP power = 250 W, CHF_3 flow = 100 SCCM, O_2 flow = 10 SCCM, Ar flow = 100 SCCM, and pressure = 20 mTorr showed a sufficiently improved etching selectivity as the AlO_x layer remained when SiN_x was etched through (Fig. 3). However, we found that after removing the remaining AlO_x layer, the surface was also damaged, suggesting the neck area between neighboring pores was too small. Despite the good etching selectivity, a gentle condition with the protection of the necks was needed to achieve a flat surface morphology, allowing the pore size at the top of the SiN_x layer to be as small as possible. We incorporated C_4F_8 gas into the etching chemistry to increase the carbon fraction in the gas and

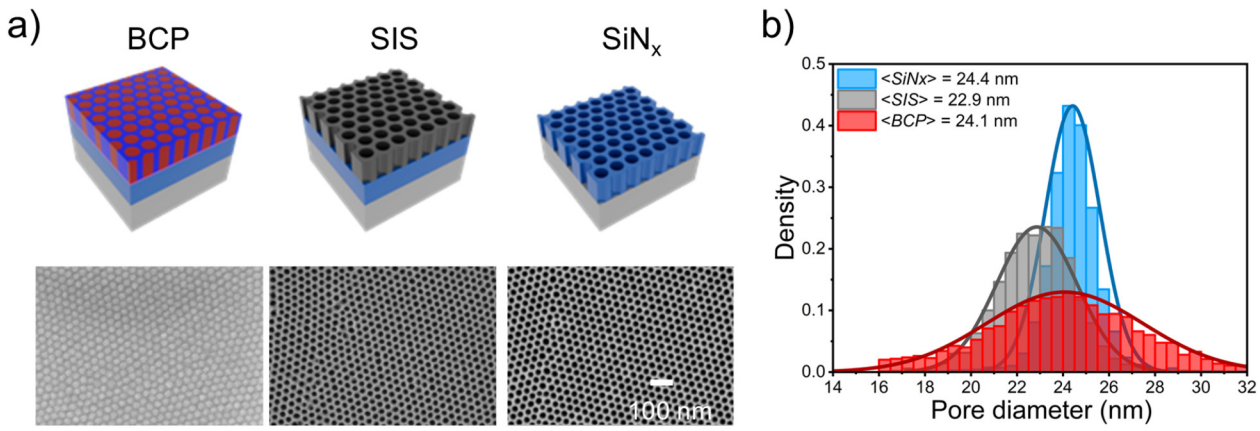

FIG. 2. (a) SEM images of the block copolymer, SIS structure after removing PS block, and etched SiN_x after removing the SIS layer. (b) Statistical analysis of the pore-size distribution based on ten SEM images of BCP, SIS pores, and SiN_x pores. The distributions of pore diameters are fitted using a normal distribution (curves).

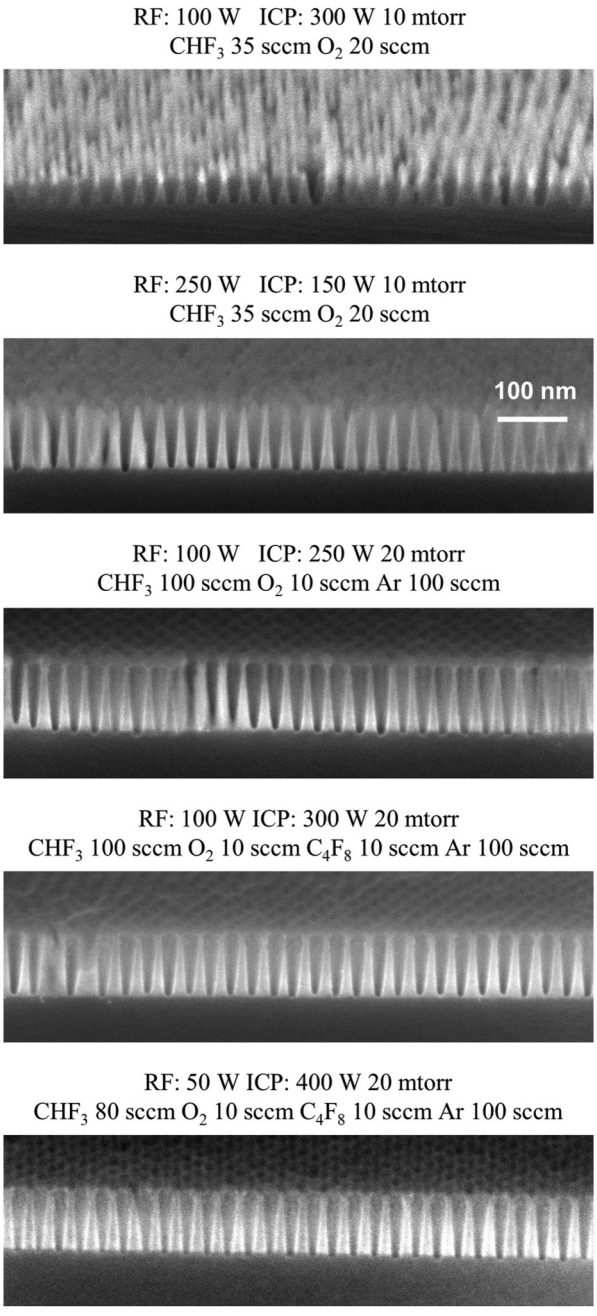

FIG. 3. Cross-sectional SEM images of SiN_x etched under different conditions with a template made with five-cycle SIS AlO_x nanopores. Etching time was determined by the complete etching of the SiN_x witness samples.

optimized the plasma power. The comparison of postetching profile is shown in Fig. 3. A SiN_x porous structure with a flat surface was achieved, as shown in the top-down SEM image in Fig. 2(a).

B. Design of back etching

A schematic of the membrane release process is shown in Fig. 1(c). A double-sided low-stress SiN_x wafer was used to create the geometric pattern necessary for releasing porous SiN_x membranes on the front side. The thickness of the SiN_x wafer was $500 \pm 25\,\mu$m. Si can be etched anisotropically in a KOH solution,[26] forming a 54.7° angle relative to the ⟨111⟩ plane, which is the wafer surface. Using CF_4/O_2 gas to remove the 100 nm SiN_x film on the back side window, the exposed Si was etched along the wafer thickness until it reached the front SiN_x layer, which was resistant to the KOH etch. The relationship between the front side length L_{front} and the backside length L_{back} can be expressed as

$$L_{front} = L_{back} - 2t/\tan(54.7^\circ), \quad (1)$$

where t is the thickness of the wafer. The designed membrane had a $5.4 \times 5.4\ mm^2$ frame size and porous area was $2.5 \times 0.7\ mm^2$ in the middle of the chip, so it required a back side window of $1.4 \times 3.2\ mm^2$. The samples were sealed to a holder before immersion in an aqueous solution of 30 wt. % KOH so that only the back side was exposed to the KOH solution. Small chips containing four membranes were used to study the etching conditions. Once validated, the etching condition was used to fabricate membranes on a 4-in. wafer, accommodating 100 membranes. Fabricating a 4-in. wafer allowed us to control the consistency, improve the yield, and minimize the process variation. Upon etching completion, the holder was rinsed with DI water and IPA to remove KOH residues and dry. The release of an unperforated SiN_x film was previously reported,[27] but we found that the same etching condition did not work for porous SiN_x. Figure 4(a) shows the SEM image of a broken porous SiN_x membrane, with a $1.4 \times 3.2\ mm^2$ back side window, etched in an 80 °C KOH solution. Therefore, optimization of the etching strategy was necessary.

Understanding the material's overall mechanical behavior under stress offers practical solutions to preventing fracture. Striemer *et al.* have taken optical micrographs of an ultrathin pnc-Si membrane at a range of applied pressures.[28] They have shown that the most strength is distributed around the edge of the membrane area. Porous structures are known to break at lower pressures than unperforated films. Thus, we have enlarged the back side window design of the membranes to create an extra $50\,\mu$m frame around the porous area at the front side such that the stress of the film can be more distributed on the nonporous SiN_x area.

It is crucial to comprehend the mechanical properties of porous SiN_x membranes for etching practices. Studies have indicated that the breakdown pressure of a porous structure can be calculated as[29]

$$P_{max} = 0.58 \times \frac{h\sigma_{yield}^{\frac{3}{2}}}{dE^{\frac{1}{2}}}(1-k), \quad (2)$$

where σ_{yield} is the yield stress, E is Young's modulus, k is the porosity, h is the thickness, and d is the length of the membrane area. For $\sigma_{yield} = 4$ GPa, $E = 290$ GPa, pore radius = 8.5 nm, pore-to-pore distance = 35 nm, $h = 100$ nm, and $d = 0.7$ mm, the breakdown pressure of the membrane is calculated to be 21 420 Pa (~3.1 psi). This

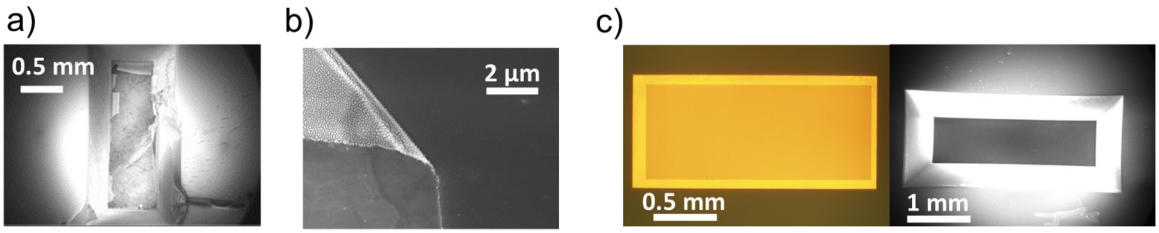

FIG. 4. (a) SEM image of a broken membrane without any protection on the front after KOH etching at 80 °C. (b) SEM image of a membrane with 200 nm PMMA on top but no adhesion layer after KOH etching at 80 °C. The protection layer is peeled off from the membrane surface. (c) Optical and SEM images of a membrane released successfully after removing the protection and adhesion layer.

relatively low breakdown pressure can be attributed to the high porosity and large floating area of the membrane. When KOH reacts with Si, it generates hydrogen bubbles. As the KOH etches through the Si layer and reaches the porous SiN_x layer, the gas needs to overcome capillary forces to penetrate through the film to the front surface. The required bubble-point pressure P_b is calculated with[30]

$$P_b = \frac{4\gamma \cos\theta}{d}, \tag{3}$$

where γ is the surface tension of solution (~0.075 N/m), θ is the liquid-solid contact angle, and d is the diameter of the pores. If we assume $\theta = 0$, $P_b = 1.7$ MPa (~2.6 kpsi), which is significantly higher than the breakdown pressure. Therefore, a protective layer is necessary to prevent gas penetration through the pores at the end of the etching process.

Initial KOH wet etching tests involved a variety of materials and adhesion layers. A 200 nm thick film of PMMA resist was deposited on a silicon chip and immersed in a 30 wt. % KOH solution at 50 °C for 5 min. Due to insufficient adhesion between the polymer film and the SiN_x surface, the PMMA layer peeled off from the SiN_x surface, as depicted in Figs. 4(b) and S4 in the supplementary material. Subsequently, a 200 nm PMMA layer with hexamethyldisilazane (HMDS) as an adhesion layer and cross-linked PS without an adhesion layer were tested under the same conditions. While peeling of PMMA was suppressed using HMDS as an adhesion layer, it was not fully prevented. Cross-linked PS, however, was eroded by the KOH solution, creating microholes on the film surfaces. Further experiments examined different adhesion layers. PMMA resist with a range of thicknesses served as a protective layer, with ProTEK primer and HMDS used as adhesion layers to Si. As shown in Fig. S5 in the supplementary material, the combination of PMMA and PEOTEK exhibited no significant changes in film morphology and color, whereas all PMMA on HMDS samples had noticeable alterations in film morphology after etching in 30 wt. % KOH at 50 °C for 45 min.

Finally, upon completion of the isoporous structure fabrication, a ProTEK primer was deposited on the SiN_x frontside surface and annealed at 205 °C for 1 min, as recommended by the vendor. Next, a 400 nm layer of PMMA resist was deposited on the same side as a protective layer. The wafer was then assembled into the KOH etching holder, exposing only the back side to the 80 °C KOH solution for approximately 5 h. After etching, clear membrane windows were observed without any bubble formation. The released wafer was further cleaned with O_2 plasma to remove the protective layer and the adhesion layer. Optical and SEM images of the membrane after dicing were taken, as shown in Fig. 4(c), where both the nonporous frame region and the porous membrane region were readily observable.

C. Analysis of pore-size distribution

The evolution of pore-size distribution from BCP scaffolds to SiN_x membranes was studied. At each process step, a set of ten SEM images, with known pixel size, were taken and analyzed using a customized MATLAB code, without bandpass filtering or image smoothing.[31] The MATLAB code employed a method called multilevel image thresholding to form a binary image, segmenting the image into multiple intensity classes by defining threshold values. Applying the same threshold standard to all images ensured that no artificial errors were introduced in the analysis. After excluding pores at the image edge, once a pore was identified, the number of pixels was counted and converted into the pore area and radius. The lower pore diameter limit was set to 8 nm for all samples, with no upper size limit. The pore-size information from the ten SEM images is displayed as a histogram in Fig. 2(b), encompassing the analysis of nearly 5000 pores. The histogram for each sample was fitted with a normal distribution, represented by the solid line.

From the fitting results, we concluded that the pore diameter distributions of BCP, SIS AlO_x after removing the PS cylinders, and front side of SiN_x nanostructures were 24.1 ± 3.4, 22.9 ± 1.8, 24.4 ± 1.2 nm (all measurements are shown as mean diameter ± standard deviation), respectively. The variation in the pore size primarily resulted from the actual variability in the BCP film, which included thermodynamic variation and defects at grain boundaries. While the diameter of the three structures remained similar, their standard deviations varied significantly, decreasing along the fabrication steps. The pore-size distribution largely depended on the SEM image quality, which required sufficiently high contrast between the matrix and the pores. The resolution of the BCP images was poor compared to AlO_x and SiN_x because of the low atomic number elements, resulting in low inherent contrast and a higher standard deviation for the BCP samples. The pore size of the SIS AlO_x not only depended on the volume fraction of the

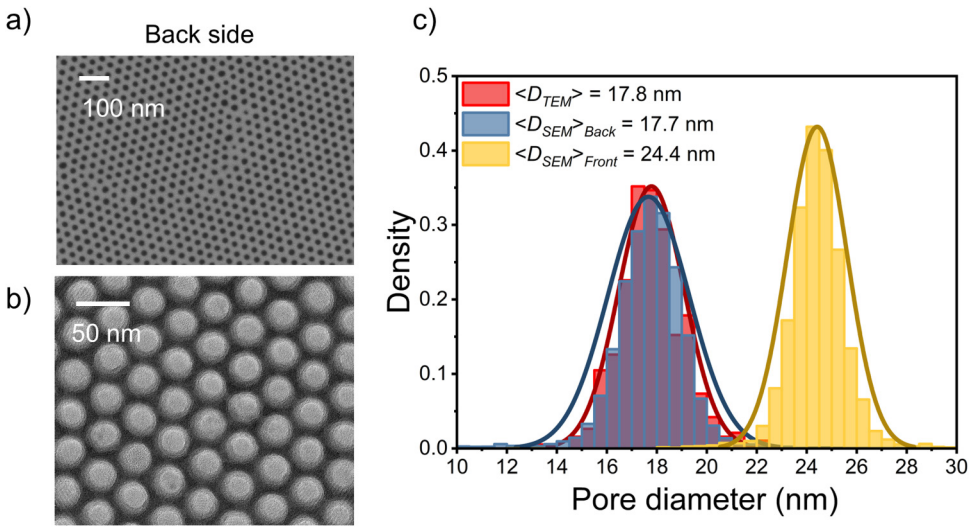

FIG. 5. (a) SEM images of the isoporous membrane sides. (b) TEM image of the isoporous membrane. (c) Statistical analysis of the pore-size distribution based on ten TEM images, and front and back side SEM images, respectively. The distributions of pore diameters are fitted using a normal distribution (curves).

PMMA block but also the amount of AlO_x infiltrated into the BCP film during SIS. Thus, the SIS AlO_x structure exhibited a smaller size compared to the BCP due to the expansion of the PMMA film after AlO_x growth, consistent with a previous study.[32] The pore size increased from the AlO_x structure to the SiN_x front side. This increase in pore size can be attributed to the etching mechanism, where the etchant not only removes material vertically but also laterally, thereby widening the pores as it progresses from the AlO_x mask to the SiN_x layer.

In addition to inspecting the SiN_x front side, SEM images of the membrane's back side and TEM images were also taken and analyzed, as depicted in Fig. 5(a). A customized TEM holder was used to directly assemble the 500 μm-thick SiN_x chip for inspection. The sample was tilted to ensure that the electron beam was perpendicular to the surface, and the focus depth was adjusted on the back side pore ends to obtain images with clear edges. The TEM images were characterized manually because the MATLAB code could not identify the edges based on the grayscale difference. ImageJ was used to manually draw ellipses covering each pore area. Over 300 ellipse sizes were collected to represent the membrane pore-size distribution. Histograms of pore-size distribution from SEM images of the membrane's front and back sides, as well as TEM images, are plotted in Fig. 5(b). The SiN_x backside pores were 17.7 ± 1.6 nm in diameter, and the TEM images showed a size of 17.8 ± 1.3 nm. The pore-size analysis of TEM and SEM images showed quantitative agreement, validating the accuracy of the MATLAB analysis and giving confidence in autoprocessing the porous structure. Compared to SEM pores, the TEM image analysis had a narrower distribution, which was partly due to the higher resolution of TEM images compared to SEM. The thresholding method of the MATLAB analysis can be further improved for higher precision.

D. Directed self-assembly

DSA of BCPs has been extensively studied to achieve density multiplication, long-range regularity, and defect elimination.[33–35] The perfection of DSA requires the prepattern, typically created using E-beam lithography, to be nearly commensurate with the BCP chemistry and morphology, allowing for the precise regulation of domain orientation. Ruiz *et al.* compared the size variation and dot displacement between the guiding spot of the prepattern and the corresponding BCP film.[36] They found that DSA of a BCP not only narrowed the size distribution from the guided pattern but also showed long-range order. To verify that DSA can be used to fabricate templates SiN_x isoporous membranes with long-range order and narrow pore-size distribution, we studied the DSA of PS-*b*-PMMA (20–59 k) over an area of 2500 × 700 μm^2.

PS-*b*-PMMA with a similar molecular weight and chemistry for achieving DSA has been reported in previous studies.[22] We employed the same fabrication process to create the chemical prepattern. A 1000 × 1000 array of hexagonally packed holes with varying dot-to-dot distances (L_s) was prepared using E-beam lithography. The density of the DSA cylinders (period L_0) was four times that of the E-beam prepatterns L_s. The size of the holes was controlled by adjusting the dose at each hole, increasing with higher doses. The HCP nanoarray in the resist was transferred into a 9 nm thick chemical pattern of 60S on SiN_x through O_2 plasma etching. PS-OH was grafted to the exposed SiN_x areas to guide the growth of PS cylinders in the PS-*b*-PMMA domain. Larger holes resulted in a higher PS volume fraction in the 60S layer, shifting the nonpreferential background to a PS-preferential background. Thus, controlling the hole size after transferring into the 60S layer determined the DSA results. The final chemical prepattern with an HCP nanostructure was needed to match the porous membrane size of 2500 × 700 μm^2, necessitating the use of a high current to

quickly write the pattern. However, the current could not exceed a threshold value at which the beam spot size was larger than the largest hole size to maintain nonpreferential background. Therefore, a 10 nA current was selected to meet both requirements efficiently.

DSA can be most effectively achieved when the period L_s in the patterned spots is an integer multiple of L_0 (35 nm) of the BCP. Because of this, a preliminary DSA test was conducted using a combination of doses ranging from 1 to 3 kμC/cm^2 and L_s values from 68 to 73 nm. Figure 6(a) shows the DSA results on the chemical patterns prepared with different L_s values, while fixing the E-beam exposure dose at 2.5 kμC/cm^2. The complete layout is assembled in Fig. S6 in the supplementary material. At doses of 1 and 1.5 kμC/cm^2, all DSA patterns showed well-defined patterns except for the DSA with $L_s = 70$ nm and a dose of 1.5 kμC/cm^2. The low dose resulted in either incomplete exposure of the resist pattern or small spot sizes, which created weak registration of PS cylinders to the PS-OH brush spot. At higher doses, more conditions exhibited structural regularity, but the defects such as parallel cylinders also appeared. When the dose was 3 kμC/cm^2, all films displayed parallel structures. The presence of parallel structures indicated that the overall interfacial energy of the prepattern could not compensate for the entropy penalty required to align the PS-*b*-PMMA film with the underlying chemical pattern. As expected, when $L_s = 2L_0$, the DSA pattern exhibited the fewest defects in the SEM images at doses ranging from 1.5 to 2.5 kμC/cm^2.

The moderate e-beam exposure dose of 2 kμC/cm^2 was optimal for DSA to ensure sufficient writing of $2500 \times 700\,\mu$m^2 HCP nanoarrays. We found that after enlarging the writing area from 120×70 to $2500 \times 700\,\mu$m^2, more parallel cylinders were found in the PS-*b*-PMMA layer, as shown in Fig. S7 in the supplementary material. The parallel cylinders could not be eliminated by adjusting to a smaller dose. We hypothesized that exposing the chemical 60S under electron beam for a long time changed its surface chemistry such that it was not perfectly nonpreferential to PS-*b*-PMMA layer. Compared to perpendicular structures, the amount of parallel cylinders was not significant, and we found in a previous study that the parallel cylinders would not be transferred into SiN_x structure.[31] It remained unanswered if DSA could be used to fabricate an isoporous membrane with a narrower size distribution than SA.

A $2500 \times 700\,\mu$m^2 DSA structure was achieved using the optimized e-beam conditions as well as the commensurability of L_s with $2L_0$. Both DSA and SA regions were infiltrated with five cycles of SIS and etched into SiN_x layer simultaneously to ensure SA and DSA underwent the same processing. After washing off the AlO_x mask, SEM images of SA and DSA SiN_x pores were captured and compared to each other [Fig. 6(b)]. A 2D fast Fourier transform (FFT) was performed to evaluate the degree of regularity. The DSA pores had a symmetric hexagonal pattern with sharp peaks, while the SA regions barely had peak structures, indicating that DSA exhibited long-range order without random domain orientation.

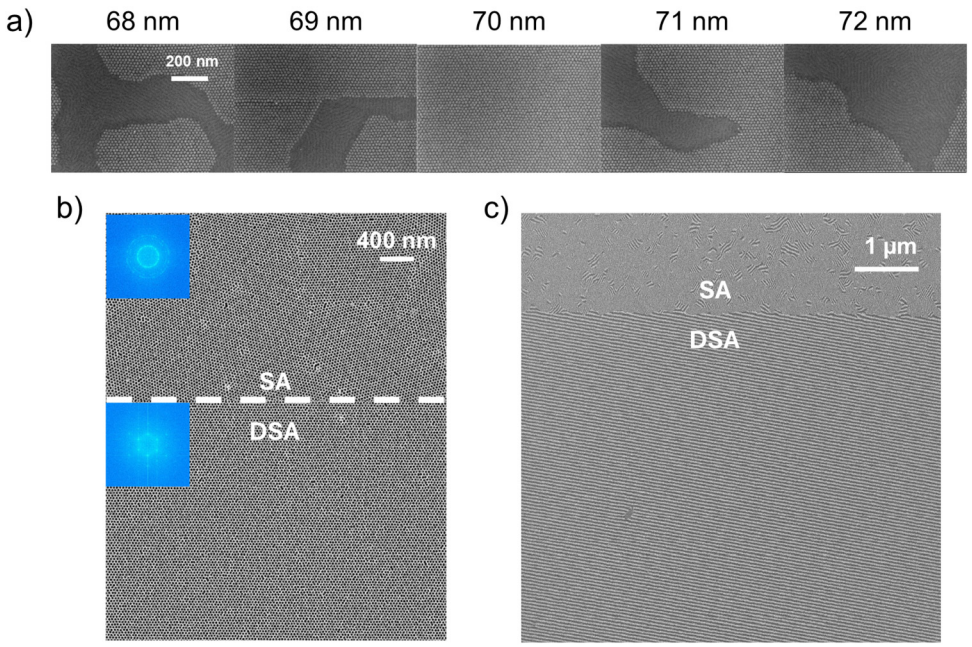

FIG. 6. (a) Top-down SEM images of the results of directed self-assembly (DSA) of PS-*b*-PMMA ($L_0 = 35$ nm) with the same dose and beam current but different registered hole-to-hole distance L_s. (b) SEM images of DSA patterns ($L_s = 70$ nm) and SA patterns etched into SiN_x, and the corresponding 2D FFT images. (c) A low-magnification SEM image of DSA ($L_s = 70$ nm) and SA patterns etched into SiN_x over a large area, taken at the edge of DSA area. The Moiré interference patterns of the DSA region are indicative of long-range order.

Figure 6(c) showed a low-magnification SEM image taken at the boundary between SA and DSA patterned SiN_x pores. Moiré interference patterns were observed in the DSA area while the SA area showed random interference patterns. However, merging pores still existed in DSA area, resulting from the lateral etching into SiN_x that expanded the pore size and the pore displacement from the HCP array. The imperfect parallel cylinders were preserved into SiN_x layer, disrupting the Moiré patterns.

The size distribution of BCP SA templated nanopores was compared with those produced by other fabrication techniques and DSA. A recent study on using DSA of PS-*b*-PMMA with similar molecular weight demonstrated that, after transferring the pores into aa SiN_x layer, the average diameter was found to be 25.3 ± 1.1 nm.[22] The size distribution of SA templated pores in this study was 24.4 ± 1.2 nm, whose standard deviation was almost identical to the DSA templated pores. This similarity suggested that we achieved a precise control over pore-size distribution with BCP SA. Verstraete *et al.* combined extreme ultraviolet (EUV) lithography with DSA to enhance the resolution of hexagonally packed holes.[37] EUV lithography alone produced pores with diameters of 16.3 ± 0.79 nm after pattern transfer etching. The self-assembled pores exhibited a similar ratio of standard deviation to diameter as those produced by EUV lithography, indicating the efficiency of BCP SA in creating large-area membranes. When EUV lithography was complemented with DSA rectification, using a 1:1 ratio between guiding dots and BCP holes, the pore size was refined to 15.6 ± 0.46 nm with a 3σ local critical dimension uniformity of 1.4. This demonstrates the capability of DSA to improve pore uniformity and reduce size variability, achieving more precise and smaller nanopores than EUV lithography alone. However, for the purposes of this study such perfection and accuracy is not necessary, and not worth the extra effort required for DSA. As a result, SA was chosen to fabricate isoporous membranes on a 4-in. wafer, rather than using DSA.

E. Flow rate measurement

The flow rate through the SiN_x isoporous membranes was measured and compared to theoretical predictions using a customized crossflow filtration system. This crossflow filtration system was specifically designed so that the majority of the fluid flows across the surface of the membrane, and a smaller amount of the fluid flows through the membrane. This design will be especially useful in future separation studies because it promotes fluid circulation over the membrane's surface, which helps to continuously remove debris and prevent the buildup of particles on the membrane, thereby ensuring that the flow rate measurements remain accurate. To prepare the SiN_x membranes, both sides were treated with O_2 plasma to remove surface contaminants and enhance hydrophilicity. After wetting the pores with IPA, the membrane was assembled into a 3D-printed cell, with channels in both the feed and permeate parts prefilled with IPA to ensure complete wetting. To protect the SiN_x membrane from damage by large particles, a polyethersulfone syringe filter with a $0.2\,\mu$m pore size was installed upstream of the 3D-printed cell. Two pressure meters were positioned at the inlet and outlet of the 3D-printed cell. The transmembrane pressure was determined by averaging the readings from these two gauges and comparing it to atmospheric pressure (permeate side). Prior to conducting the flow rate measurements, water was recirculated within the system for 24 h to stabilize the water flux at a transmembrane pressure of approximately 0.2 psi. After stabilization, pressures of 0–1.5 psi were applied, and the mass of permeate water was collected and weighed using a balance. The water flux at each pressure was calculated by measuring the change in permeate mass as a function of time and membrane area. This method provided a reliable assessment of the membrane's performance under different pressure conditions.

Figure 7 shows the water flux results from four SiN_x membranes. All four groups exhibited a linear relationship between water flux and applied pressure, suggesting stable permeability for each sample. The water flux results were compared to theoretical values predicted by the Hagen–Poiseuille equation, expressed as

$$\text{Flux} = \frac{Q}{\text{Area}} = \frac{\pi \Delta P R^4}{8\mu \text{L} \times \text{Area}}, \tag{4}$$

where Q is the volumetric flow rate, Area is the membrane area, ΔP is the transmembrane pressure, R is the pore radius, μ is the dynamic viscosity of fluid, and L is the membrane thickness. Assuming all pores contributed equally to the overall water flux without pore-to-pore interactions, the number of pores was estimated by the porosity calculated from the hexagonal geometry with $L_0 = 35$ nm. The theoretical values considered the conical pores, with the diameter of the mean front pore size equal to 17.8 nm and the mean back pore size of 24.4 nm. The measured permeability lay between the two theoretical predictions, indicating that the actual performance of the membranes was consistent with the theoretical models based on the geometric and physical properties of the pores. It further validated the idea of using this model isoporous

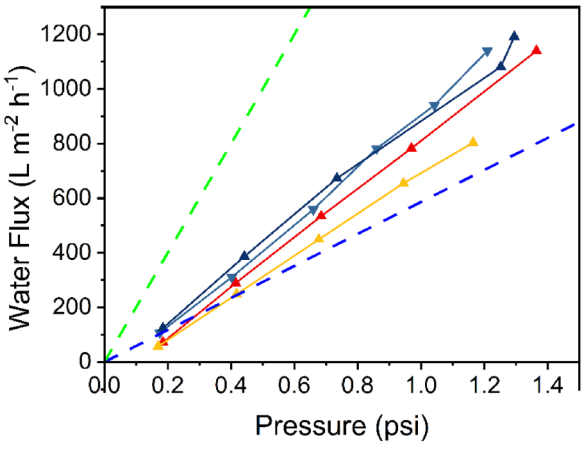

FIG. 7. Water flux through silicon nitride membranes vs applied pressure. The permeability of the membrane was calculated from the slope of the data. The water fluxes are compared with the Hagen–Poiseuille equation (dashed lines) with pore diameters of 17.8 (blue) and 24.4 nm (green).

membrane to be compared to or interpreted with the hindered transport model.

IV. SUMMARY

We successfully fabricated SiN_x porous structures templated from BCP and SIS and released the membranes into the air. Our optimization process encompassed conditions for cylinder formation in BCP and dry etching conditions to effectively transfer the mask into the SiN_x layer. Upon fabrication completion, SEM and TEM images were analyzed to study the pore-size distribution of the porous structures. The SiN_x membranes exhibited a narrow pore-size distribution, leading us to classify them as isoporous membranes. We demonstrated the DSA of BCP used in this work, which eliminated domain boundaries and enhanced long-range order. Finally, we measured the water flux through the membranes and compared it with theoretical predictions based on the Hagen–Poiseuille equation, finding excellent agreement between the experimental and theoretical results.

SUPPLEMENTARY MATERIAL

The following supplementary figures are available. SEM images of annealing 80 nm thick PS-*b*-PMMA on 60S for different times at 270 °C (Fig. S1). SEM images of annealing 90 nm thick PS-*b*-PMMA at 270 °C for 2 h on P(S-*r*-MMA) with different volume fractions of styrene (S) (Fig. S2). SEM images of annealing PS-*b*-PMMA with different thicknesses at 270 °C for 2 h on 60S (Fig. S3). Samples were prepared with different preparation methods: (a) 200 nm 495 kg/mol PMMA on Si wafer; (b) 200 nm 495 kg/mol PMMA on Si wafer with HMDS as an adhesion layer; and (c) 100 nm crosslinked PS on Si wafer. The images were taken after immersing chips in an aqueous solution of 30 wt. % KOH at 50 °C for 5 min (Fig. S4). 495 kg/mol PMMA protection layers were prepared with different thicknesses and adhesion layers. The samples were annealed at 180 °C for 5 min before immersion in an aqueous solution of 30 wt. % KOH at 50 °C for 45 min. The top row shows PMMA layers on a monolayer of HMDS with thicknesses of 135, 150, and 231 nm before etching, left to right. The bottom row shows PMMA layers on a monolayer of HMDS with thicknesses of 135, 150, 179, and 231 nm after KOH etching, left to right (Fig. S5). SEM images of the DSA results with different exposed dose and pore-to-pore distance L_s. The BCP morphologies with long-range order and perpendicular geometry are framed by the green lines (Fig. S6). SEM images of the $2500 \times 700\,\mu m^2$ DSA result at different magnifications, with a pattern writing dose of $2\,k\mu C/cm^2$ on a 9 nm 60S random copolymer layer (Fig. S7).

ACKNOWLEDGMENTS

This work was supported as part of the Advanced Materials for Energy-Water Systems (AMEWS) Center, an Energy Frontier Research Center funded by the U.S. Department of Energy, Office of Science, Basic Energy Sciences at Argonne National Laboratory under Contract No. DE-AC02-06CH11357. The Analytical Picoprobe Electron Microscope used in part of this work (ThermoFisher Scientific Spectra Ultra X) was developed as part of a CRADA #01300710 between ANL and ThermoFisher Scientific Instruments. The PicoProbe imaging was also supported by the National Science Foundation Major Research Instrumentation (MRI) Program (No. NSF DMR-2117896) at the University of Chicago. This work made use of the Pritzker Nanofabrication Facility (PNF) of the Pritzker School of Molecular Engineering at the University of Chicago.

AUTHOR DECLARATIONS

Conflict of Interest

The authors have no conflicts to disclose.

Author Contributions

Wen Chen: Conceptualization (equal); Data curation (equal); Formal analysis (equal); Methodology (equal); Writing – original draft (equal); Writing – review & editing (equal). **Soonmin Yim:** Data curation (supporting); Investigation (supporting). **Nestor J. Zaluzec:** Data curation (supporting); Methodology (supporting). **Gordon S. W. Craig:** Writing – original draft (equal); Writing – review & editing (equal). **Seth B. Darling:** Conceptualization (equal); Funding acquisition (equal); Project administration (equal). **Paul F. Nealey:** Conceptualization (equal); Funding acquisition (equal); Project administration (equal); Writing – original draft (equal); Writing – review & editing (equal).

DATA AVAILABILITY

The data that support the findings of this study are available from the corresponding author upon reasonable request.

REFERENCES

[1]A. Lee, J. W. Elam, and S. B. Darling, Environ. Sci. Water Res. Technol. **2**, 17 (2016).
[2]D. F. Sanders, Z. P. Smith, R. Guo, L. M. Robeson, J. E. McGrath, D. R. Paul, and B. D. Freeman, Polymer **54**, 4729 (2013).
[3]J. L. Anderson and J. A. Quinn, Biophys. J. **14**, 130 (1974).
[4]O. A. Kazi, W. Chen, J. G. Eatman, F. Gao, Y. Liu, Y. Wang, Z. Xia, and S. B. Darling, Adv. Mater. **35**, 2300913 (2023).
[5]W. M. Deen, AIChE J. **33**, 1409 (1987).
[6]N. Hampu, J. R. Werber, W. Y. Chan, E. C. Feinberg, and M. A. Hillmyer, ACS Nano **14**, 16446 (2020).
[7]L. Zeman and M. Wales, in *Synthetic Membranes: Volume II*, edited by A. F. Turbak (American Chemical Society, Washington, 1981), Vol. 154, p. 411.
[8]R. Z. Waldman, F. Gao, W. A. Phillip, and S. B. Darling, J. Membr. Sci. **633**, 119389 (2021).
[9]M. Mireles and T. R. Gaborski, Electrophoresis **38**, 2374 (2017).
[10]M. Lepoitevin, T. Ma, M. Bechelany, J.-M. Janot, and S. Balme, Adv. Colloid Interface Sci. **250**, 195 (2017).
[11]C. Zhou, T. Segal-Peretz, M. E. Oruc, H. S. Suh, G. Wu, and P. F. Nealey, Adv. Funct. Mater. **27**, 1701756 (2017).
[12]S. E. Querelle, E. A. Jackson, E. L. Cussler, and M. A. Hillmyer, ACS Appl. Mater. Interfaces **5**, 5044 (2013).
[13]V. Silva, P. Prádanos, L. Palacio, and A. Hernández, Desalination **245**, 606 (2009).
[14]W. A. Phillip, R. M. Dorin, J. Werner, E. M. V. Hoek, U. Wiesner, and M. Elimelech, Nano Lett. **11**, 2892 (2011).
[15]W. A. Phillip, B. O'Neill, M. Rodwogin, M. A. Hillmyer, and E. L. Cussler, ACS Appl. Mater. Interfaces **2**, 847 (2010).
[16]Y. Wang, Acc. Chem. Res. **49**, 1401 (2016).
[17]M. Müller and V. Abetz, Chem. Rev. **121**, 14189 (2021).

[18]Y.-C. Tseng, Q. Peng, L. E. Ocola, J. W. Elam, and S. B. Darling, J. Phys. Chem. C **115**, 17725 (2011).
[19]H. Feng, B. Kash, S. Yim, K. Bagchi, G. S. W. Craig, W. Chen, S. J. Rowan, and P. F. Nealey, Langmuir **39**, 14688 (2023).
[20]E. Han, K. O. Stuen, Y.-H. La, P. F. Nealey, and P. Gopalan, Macromolecules **41**, 9090 (2008).
[21]P. Mansky, T. P. Russell, C. J. Hawker, J. Mays, D. C. Cook, and S. K. Satija, Phys. Rev. Lett. **79**, 237 (1997).
[22]C. Zhou, N. Tambo, E. M. Ashley, Y. Liao, J. Shiomi, K. Takahashi, G. S. W. Craig, and P. F. Nealey, ACS Nano **14**, 6980 (2020).
[23]E. M. Ashley, P. J. Duda III, and P. F. Nealey, J. Vac. Sci. Technol. B **39**, 064005 (2021).
[24]Y.-C. Tseng, Q. Peng, L. E. Ocola, D. A. Czaplewski, J. W. Elam, and S. B. Darling, J. Vac. Sci. Technol. B **29**, 06FG01 (2011).
[25]B. J. Lee, A. Efremov, and K.-H. Kwon, Plasma Processes Polym. **18**, 2000249 (2021).
[26]T. Segal-Peretz *et al.*, ACS Nano **11**, 1307 (2017).
[27]J. Ren, L. E. Ocola, R. Divan, D. A. Czaplewski, T. Segal-Peretz, S. Xiong, R. J. Kline, C. G. Arges, and P. F. Nealey, Nanotechnology **27**, 435303 (2016).
[28]C. C. Striemer, T. R. Gaborski, J. L. McGrath, and P. M. Fauchet, Nature **445**, 749 (2007).
[29]C. van Rijn, M. van der Wekken, W. Nijdam, and M. Elwenspoek, J. Microelectromech. Syst. **6**, 48 (1997).
[30]S. Kuiper, M. d. Boer, C. v. Rijn, W. Nijdam, G. Krijnen, and M. Elwenspoek, J. Micromech. Microeng. **10**, 171 (2000).
[31]F. Gao, W. Chen, J. G. Eatman, R. Z. Waldman, N. J. Zaluzec, R. Dong, P. F. Nealey, and S. B. Darling, Nat. Water **2**, 521 (2024).
[32]T. Segal-Peretz *et al.*, ACS Nano **9**, 5333 (2015).
[33]S.-M. Park, G. S. W. Craig, C.-C. Liu, Y.-H. La, N. J. Ferrier, and P. F. Nealey, Macromolecules **41**, 9118 (2008).
[34]C.-C. Liu *et al.*, Macromolecules **46**, 1415 (2013).
[35]S. B. Darling, Prog. Polym. Sci. **32**, 1152 (2007).
[36]R. Ruiz, H. Kang, F. A. Detcheverry, E. Dobisz, D. S. Kercher, T. R. Albrecht, J. J. de Pablo, and P. F. Nealey, Science **321**, 936 (2008).
[37]L. Verstraete, H. S. Suh, J. Van Bel, B.-U. Bak, S. E. Kim, R. Vallat, P. Bezard, M. Beggiato, and C. Beral, *Material and Process Optimization for EUV Pattern Rectification by DSA* (SPIE, San Jose, CA, 2024).